



Extended Kalman filter method for state of charge estimation of vanadium redox flow battery using thermal-dependent electrical model



Binyu Xiong^a, Jiyun Zhao^{a,*}, Zhongbao Wei^a, Maria Skyllas-Kazacos^b

^a EXQUISITUS, Centre for E-City, School of Electrical & Electronic Engineering, Nanyang Technological University, Singapore 639798, Singapore

^b School of Chemical Engineering, The University of New South Wales, UNSW Sydney, NSW 2052, Australia

HIGHLIGHTS

- A novel state of charge estimation method, extended Kalman filter, is proposed.
- A thermal-dependent electrical model is established for vanadium flow battery.
- An open circuit flow cell in each stack for measurement can be saved.
- The robustness of EKF method is evaluated under lab and online operation scenarios.
- State of charge estimation methods are reviewed and compared.

ARTICLE INFO

Article history:

Received 4 March 2014

Received in revised form

21 March 2014

Accepted 22 March 2014

Available online 29 March 2014

Keywords:

Vanadium redox flow battery

State of charge

Extended Kalman filter

Thermal dependent electrical model

Flow rate

Temperature

ABSTRACT

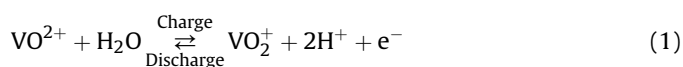
State of charge (SOC) estimation is a key issue for battery management since an accurate estimation method can ensure safe operation and prevent the over-charge/discharge of a battery. Traditionally, open circuit voltage (OCV) method is utilized to estimate the stack SOC and one open flow cell is needed in each battery stack [1,2]. In this paper, an alternative method, extended Kalman filter (EKF) method, is proposed for SOC estimation for VRBs. By measuring the stack terminal voltages and applied currents, SOC can be predicted with a state estimator instead of an additional open circuit flow cell. To implement EKF estimator, an electrical model is required for battery analysis. A thermal-dependent electrical circuit model is proposed to describe the charge/discharge characteristics of the VRB. Two scenarios are tested for the robustness of the EKF. For the lab testing scenarios, the filtered stack voltage tracks the experimental data despite the model errors. For the online operation, the simulated temperature rise is observed and the maximum SOC error is within 5.5%. It is concluded that EKF method is capable of accurately predicting SOC using stack terminal voltages and applied currents in the absence of an open flow cell for OCV measurement.

© 2014 Elsevier B.V. All rights reserved.

1. Introduction

Redox flow batteries have emerged as competitive alternatives for large scale energy storage over traditional batteries such as lead acid batteries and lithium iron phosphate batteries coupled with renewable energy sources in micro-grids for reliable power delivery. After years of development, vanadium redox flow batteries (VRBs) invented in 1980s by Skyllas-Kazacos and co-workers [3,4] at the University of New South Wales have gained a high

reputation and have reached successful commercialization among other flow batteries by the virtue of favorable benefits such as long operation lifetime, elimination of electrolyte cross-contamination, power/capacity design independence, high battery efficiency, inflammable and nontoxic electrolyte [5–7]. The battery distinguishes itself by employing V(II)/V(III) and V(IV)/V(V) species in the sulfuric acid and the half-cell reactions on positive and negative electrodes are shown respectively below,



* Corresponding author. Tel.: +65 6790 4508; fax: +65 6793 3318.

E-mail address: jyzhao@ntu.edu.sg (J. Zhao).

Nomenclature		V	volume of stack or tank (L)
c	vanadium concentration (mol L ⁻¹)	<i>Greek symbol</i>	
u	input	η_{con}	concentration overpotential (V)
z	number of electron transferred in reaction	ρ	electrolyte density (K gm ⁻³)
x	battery state	θ	polypropylene thickness (m)
A	electrode area (m ²)	ν	mean velocity in the channel (ms ⁻¹)
C_p	specific heat of electrolyte (J Kg ⁻¹ K ⁻¹)	κ	diffusion layer
E^\ominus	formal electrode potential (V)	γ	activity coefficient
F	faraday constant (C mol ⁻¹)	<i>Subscript</i>	
H	heat convection coefficient (W m ⁻² K ⁻¹)	ch	chemical reaction
H^\ominus	standard molar enthalpy (J mol ⁻¹)	min	minimal flow rate
I	current (A)	cell	cells in stack
M_t	local mass transfer coefficient	c	charging
N	number of cells	d	discharging
P	power (W)	i	vanadium species
P_k	prediction covariance	p	pipe
Q	flow rate (cm ³ s ⁻¹)	R	resistance
Q_k	covariance of observation noise	s	stack
R	gas constant (J K ⁻¹ mol ⁻¹)	t	tank
R_k	covariance of process noise	+	positive side
S^\ominus	standard molar reaction entropy (J K ⁻¹)	–	negative side
SOC	state of charge (%)		
T	temperature (°C)		



The developments of various VRB models are useful for multiple purposes. For battery stack design and scale-up, a two dimensional electrochemical model based on the conservation law of mass, charge and momentum transport was developed by Shah [8–10]. The comprehensive models are solved by finite element method and are capable of predicting profiles of overpotential, current density, temperature and concentration within a cell unit. Later, Knehr [11] extended the 2D isothermal model by accounting for the species crossover phenomenon and side reactions, which further improved the accuracy of the existing model. Since the electrochemical reactions and mass transfer equations are highly coupled, M. Vynnycky [12] proposed an asymptotically reduced model to considerably lower the computational requirements yet preserve the model accuracy. Although these models exhibit detailed information and give insights for battery design, they are inappropriate for real time monitoring and control due to the complexity and long computation time. To facilitate the system-level design and control of interfacing devices like electronic converters, a control-oriented electrical model is essential. Only a few models have been developed from this perspective. An equivalent electrical circuit model for a unit cell was presented by Mohamed in Ref. [13]. The model consists of two pairs of Resistor–Capacitor series and open-circuit voltage representing the dynamic behavior and polarization effect. An Extend Kalman filter algorithm is implemented for the RC network parameter identification with experimental data. Yu [14] developed a dynamic model of a vanadium redox flow battery for system control incorporating mass transfer and ion crossover effects. Tang et al. developed several thermal models in predicting the electrolyte temperature change including self-discharge and shunt current [15–17]. These papers show that the temperature rise of electrolyte is clearly observed during operation especially for high power rating stack and fast electrolyte flow rates. The temperature variation would influence terminal voltage and diffusion rates of membrane and thus the performance of battery. In previous

models, thermal modeling and electrical modeling are not incorporated for high power rating VRB stacks.

Monitoring the state of charge (SOC) of a battery is a critical issue for battery management in terms of long-term and real-time operation. For long-term operation of VRB, the problem of electrolyte imbalance due to different transfer rates of ions between two half-cells arises, which leads to the loss of capacity. Thus, electrolyte rebalancing systems need to be developed based on the observance of SOC of each half-cell. Two methods, the utilization of electrolyte conductivity measurements and spectrophotometric properties, were proposed by Kazacos and Skyllas-Kazacos [1]. Later, the two half-cell solution potentials were further calibrated for SOC monitoring by Corcuera and Skyllas-Kazacos [18]. Other research teams [19–21] adapted and improved these three methods in different ways. By detecting the transmission spectrum of the positive electrolyte, L. Liu [19] developed a new method for monitoring the SOC of the VRB. Rudolph [20] used identical IR optical sensors to allow the independent SOC measurement within the accuracy of $\pm 1\%$. For real-time operation, the instantaneous SOC as a function of remaining capacity needs to be monitored to avoid exceeding charging/discharging all the time. The instantaneous SOC reflects the battery capacity remain under the assumption of balanced electrolytes in both positive and negative cells.

The open circuit voltage (OCV) method is a simple method and widely implemented for real-time SOC monitoring in commercial products. The corresponding SOC is obtained by a predetermined relationship based on terminal voltages of an open flow cell. Usually a corrected Nernst Equation is applied to describe this relationship [2]. Despite its simplicity, OCV is affected by factors such as temperature and flow rate, the fluctuation of which may result in large prediction errors. Moreover, this method makes stack configuration more complex since one open flow cell needs to be spared for each stack and additional voltage sensors are to be installed. A typical stack structure with one open flow cell for OCV measurement is shown in Fig. 1.

Apart from the OCV method, the extended Kalman filter (EKF) method is widely adopted in traditional battery systems. In the

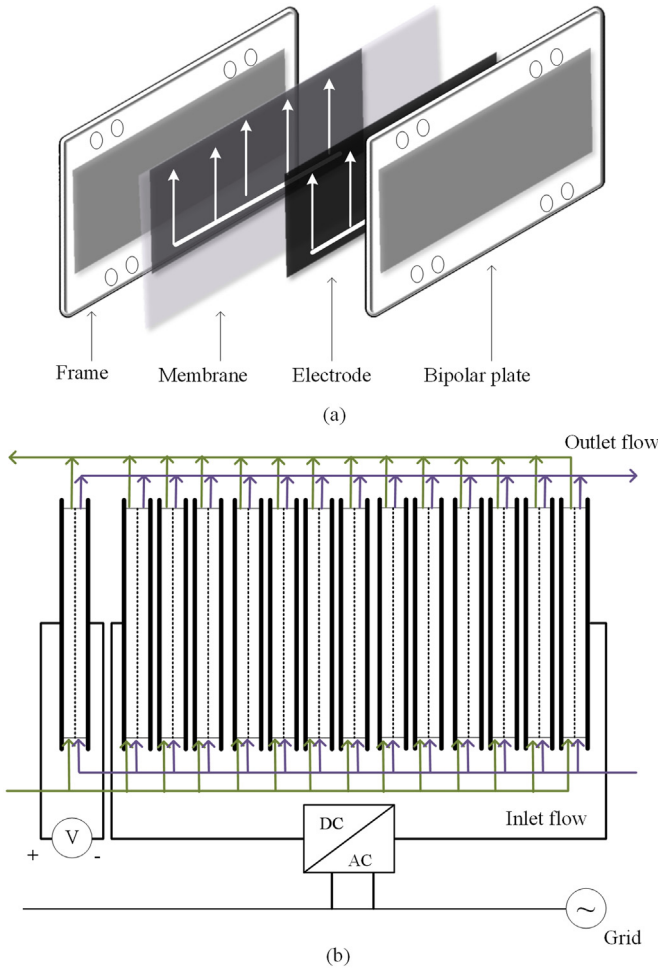


Fig. 1. One cell structure and open-circuit voltage measurement method (a) single cell structure (b) stack structure with one open flow cell.

absence of one open flow cell and additional sensors, EKF provides accurate prediction of instantaneous SOC according to the measured stack terminal voltage and current. Plett [22–24] gave a review of EKF method for battery management system of lithium-ion polymer battery packs. Mastali [25] implemented a dual extended Kalman filter to predict the SOC of batteries with different geometries. Xiong [26,27] set up a complete dynamic polarization battery model and estimated both SOC and peak power capability with adaptive EKF method. Chiang [28] further estimated the ultracapacitor SOC with an extended electrical model including temperature effect. So far, the EKF method has not been investigated for SOC estimation of VRB systems during real-time operation.

In this paper, a thermal-dependent electrical model is firstly proposed for battery control. The model integrates the effect of temperature and flow rate, which are two major factors affecting the battery terminal voltages. The EKF method is then utilized to predict real-time SOC based on the newly proposed model. The model is validated by experimental data and the accuracy of SOC estimation based on KEF is tested and discussed.

2. Thermal-dependent electrical model development

An accurate model is essential for a reliable battery state estimation. Therefore, an equivalent electrical model that considers the

effects of temperature and flow rate is initially set up. Diagram of the proposed model is shown in Fig. 2. The model consists of four parts, an open circuit voltage source, charging/discharging internal resistances, a temperature prediction model and concentration overpotential unit. The four parts are elaborated in the following sections.

2.1. Open circuit voltage

The open circuit voltage represents the battery electromotive force at the ideal state, which is related to vanadium ion concentration and temperature. In electrochemistry, electrode potential, E , is determined by the Nernst Equation given by [29],

$$E = E^\ominus + \frac{RT}{zF} \ln \left(\frac{c_{V^{2+}} c_{VO_2^+} c_{H^+}^2}{c_{VO^{2+}} c_{V^{3+}}} \cdot \frac{\gamma_{V^{2+}} \gamma_{VO_2^+} \gamma_{H^+}^2}{\gamma_{VO^{2+}} \gamma_{V^{3+}}} \right) \quad (3)$$

where E^\ominus denotes the formal electrode potential. C_i denotes the vanadium ion concentration. γ is the activity coefficient for the species.

The battery SOC is related to the vanadium ion concentration by the definition

$$SOC = \frac{c_{V^{2+},t}}{c_{V^{2+},t} + c_{V^{3+},t}} = \frac{c_{VO_2^+,t}}{c_{VO_2^+,t} + c_{VO^{2+},t}} \quad (4)$$

where $c_{i,t}$ is the vanadium ions concentration in the tanks.

The concentration of protons in the catholyte is hard to estimate due to the ion pairing equilibrium in the solutions, and usually the proton concentration is considered as 1 M. Alternatively, it is assumed to remain constant and is incorporated into the formal potential that is experimentally measured at 50% SOC [18]. The second term of activity coefficient product in brackets is approximately to be 1 since the cancellation of each species, but can also be incorporated into the experimentally determined formal potential. By substituting Eq. (4) into Eq. (3), the Nernst equation is simplified as,

$$E = E^\ominus + \frac{2RT}{zF} \ln \left(\frac{SOC}{1 - SOC} \right) \quad (5)$$

By comparison of experimental data [2,30] and the simulated OCV curves using a formal potential of 1.39 V [18] in Fig. 3, the Nernst equation in Eq. (5) shows good agreement with the experimental data with a maximum relative error of 3.5%. The figure illustrates OCV curves with respect to two different conditions of temperature and vanadium ion concentrations. Although the vanadium ion concentration in Fig. 3(a) is twice of that in Fig. 3(b), OCV is not doubled and the characteristics are similar according to the ratio of concentration in the positive and negative electrolytes. This validates that the Nernst equation is able to describe the behavior of OCV at large extend of SOC where activation and concentration overpotentials are not predominant.

2.2. Temperature prediction model

For large power rating VRB stacks, temperature change is not negligible due to the large amount of heat accumulation during high power operation. This effect influences the electrolyte stability as well as electrochemical properties, such as the membrane diffusion rate, electrolyte viscosity, activation overpotential, and ohmic overpotential. From the Nernst equation in Eq. (5), OCV is also affected by temperature. Besides, according to chemical thermodynamics, formal potential E^\ominus is dependent with temperature described in Eq. (6),

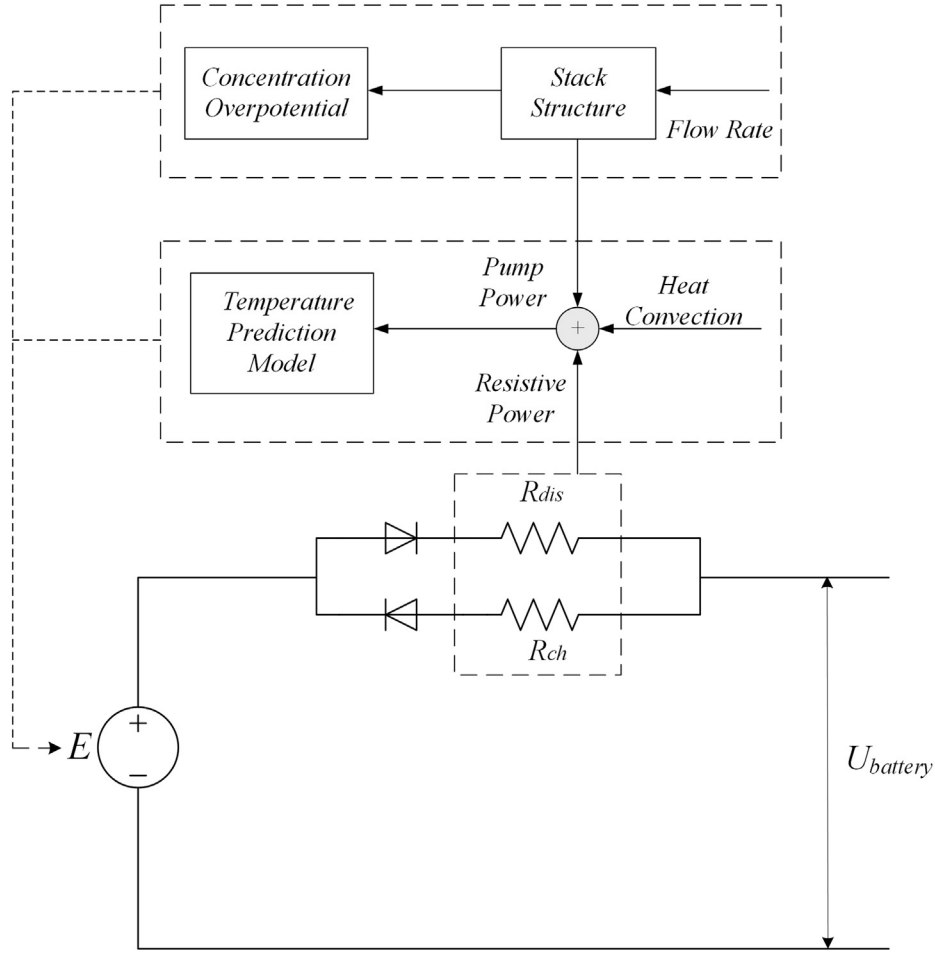


Fig. 2. Thermal-dependent electrical model of vanadium redox flow battery.

$$\frac{dE^\ominus}{dT} = -\frac{1}{zF} \left(\frac{d\Delta G^\ominus}{dT} \right) = -\frac{1}{zF} \left(\frac{d\Delta H^\ominus}{dT} - \Delta S^\ominus \right) \quad (6)$$

where ΔS^\ominus is the molar reaction entropy. ΔG^\ominus is the molar Gibbs free reaction enthalpy. ΔH^\ominus is the molar reaction enthalpy. The thermodynamic values are listed in Ref. [31]. Heintz and Illenberger [32] have determined the relationship between the formal potential and temperature.

A negative slope of 1.62 mV K^{-1} between 5°C and 50°C is found experimentally.

Combined with Eq. (5), the derivative of OCV with respect to temperature can be expressed as,

$$\frac{dE}{dT} = -\frac{1}{zF} \left(\frac{d\Delta H^\ominus}{dT} - \Delta S^\ominus \right) + \frac{2R}{zF} \ln \left(\frac{\text{SOC}}{1 - \text{SOC}} \right) \quad (7)$$

Electrolyte temperature rise is attributed to heat generation factors including chemical reaction heat release, internal resistance power loss and pump power loss during operation. Once temperature rise is obtained, the change of OCV will be found. The thermal dynamics of the electrolyte is described by a temperature prediction model which is discussed in detail in Ref. [31]. Defining the temperature variation, ΔT_i ,

$$\Delta T_i = T_i - T_{\text{air}}.$$

where i denotes stack, pipes or tanks. Based on energy conservation law, the temperature variations of the electrolytes are formulated as,

For stack temperature variation,

$$C_p \rho V_s \frac{dT_s}{dt} = Q_+ C_p \rho (\Delta T_{p+} - \Delta T_s) + Q_- C_p \rho (\Delta T_{p-} - \Delta T_s) + H_s A_s (-\Delta T_s) + P_R + P_{ch} \quad (8)$$

For pipe temperature variation,

$$C_p \rho V_p \frac{dT_{p+}}{dt} = Q_+ C_p \rho (\Delta T_{t+} - \Delta T_{p+}) + Q_+ C_p \rho (\Delta T_s - \Delta T_{p+}) + H_p A_p (-\Delta T_{p+}) + P_{\text{pump}+} \quad (9)$$

$$C_p \rho V_p \frac{dT_{p-}}{dt} = Q_- C_p \rho (\Delta T_{t-} - \Delta T_{p-}) + Q_- C_p \rho (\Delta T_s - \Delta T_{p-}) + H_p A_p (-\Delta T_{p-}) + P_{\text{pump}-} \quad (10)$$

For tank temperature variation,

$$C_p \rho V_{t+} \frac{dT_{t+}}{dt} = Q_+ C_p \rho (\Delta T_{p+} - \Delta T_{t+}) + H_t A_t (-\Delta T_{t+}) \quad (11)$$

$$C_p \rho V_{t-} \frac{dT_{t-}}{dt} = Q_- C_p \rho (\Delta T_{p-} - \Delta T_{t-}) + H_t A_t (-\Delta T_{t-}) \quad (12)$$

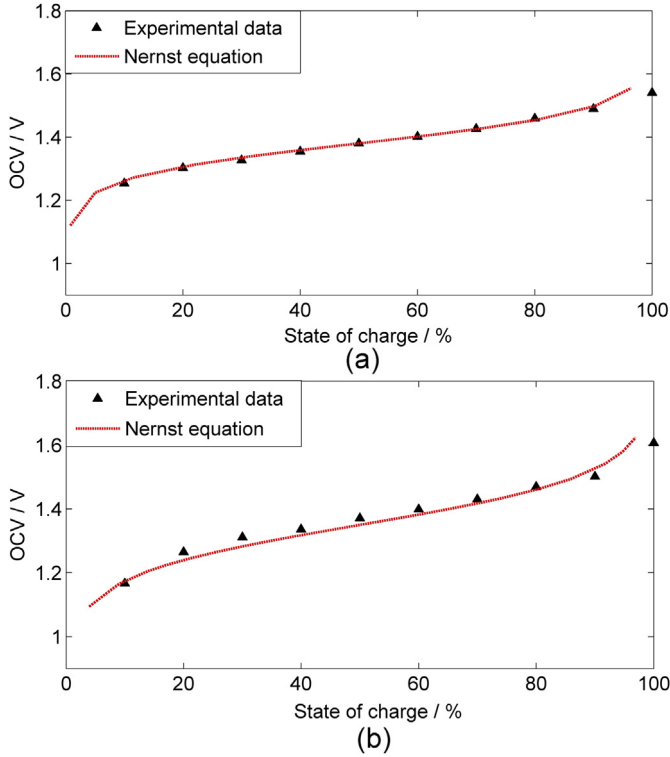


Fig. 3. Comparison of experimental OCV and predicted OCV by Nernst equation (a) $T = 303$ K, $c = 2$ M, (b) $T = 298$ K, $c = 1$ M.

where ΔT_s , ΔT_p , ΔT_t denote the temperature rise in the stack, pipes, and tanks respectively.

P_R is the ohmic overpotential loss in the stack which depends on the value of internal resistance of electrolyte, membrane and electrodes. The ohmic power loss is linked with applied current as according to $P_R = I^2 R$.

P_{ch} denotes the chemical reaction heat generation/absorption during the charge/discharge process. The entropic heat can be expressed as [33],

$$P_{ch} = IT \frac{dE}{dT} = \frac{IT}{zF} \left[\Delta S_r^\theta + R \ln \left(\frac{c_{VO_2^+} c_{V^{2+}} c_{H^+}^2}{c_{VO^{2+}} c_{V^{3+}}} \right) \right] \quad (13)$$

P_{pump} is the pump power loss due to the viscosity of circulation. The following equation can be used to evaluate the pump power:

$$P_{pump} = \Delta p \times Q \quad (14)$$

where Δp is the pressure drop in the stack and pipe circuit caused by hydraulic resistance, Q is the operating flow rate.

$H_s A_s$ represents heat transfer in terms of nature convection at the stack.

From the above model, the thermal effect on voltage is described in Eq. (7) and temperature variation can be obtained by solving Eqs. (8)–(12).

2.3. Concentration overpotential unit

Distinguished from traditional batteries, flow rate is a unique parameter for flow batteries involving mass transport within the stack. Active species are transferred to the electrode surface by diffusion, migration and convection which are all limited by the flow rate. The concentration overpotential is due to the

concentration difference in the diffusion layer between the bulk solution and the electrode surface. This overpotential is particularly significant at the end of charge/discharge process since the active vanadium ion concentrations are low, and may result in premature cut-off in stack voltage control at low flow rate. Therefore, a concentration overpotential term as a function of flow rate is considered in this model.

In recent study, A. Tang [34] used a compact expression for the concentration overpotential as,

$$\eta_{con}^{+,-} = \frac{RT}{F} \ln \left(\frac{c_0}{c_b} \right) \quad (15)$$

where C_0 and C_b are the reactant concentrations at the surface and in the bulk solution respectively for each half cell. From Fick's first law which relates the diffusive flux to the electrode surface under steady state, the diffusion rate and diffusion layer can be derived as,

$$\frac{D}{\kappa} = \frac{I}{zF(c_b - c_0)} \quad (16)$$

where D denotes the diffusion coefficient, κ is the thickness of diffusion layer. I is the applied current.

Defining the local mass transfer coefficient, M_t , as,

$$M_t = \frac{D}{\kappa} \quad (17)$$

The local mass transfer coefficient at electrode surface can be linked with the velocity of electrolyte flow, v , by [35],

$$M_t = 1.6 \times 10^{-4} v^{0.4} \quad (18)$$

By solving Eqs. (15)–(18), the overpotential is expressed as,

$$\eta_{con}^{+,-} = \frac{RT}{F} \ln \left(1 - \frac{I}{1.6 \times 10^{-4} z(Q/A)^{0.4} c_b} \right) \quad (19)$$

This is in agreement with the concentration overpotential term used by Tang et al. in their VRB model [34].

2.4. Internal resistance

In a flow battery cell, the internal resistances during charge and discharge, R_c , R_d , include the ohmic losses of the electrodes, membrane, and electrolyte which can be measured experimentally. Materials have a significant impact on internal resistances and various types of electrodes and membranes have been evaluated in Refs. [36–38]. Since the membrane and electrodes contribute most to the cell resistivity, it is necessary to select proper materials with small resistance and long cycle life in the stack design. Furthermore, a small interelectrode distance is also needed to reduce the ohmic drop through the cell.

After introducing four parts in the model, the overall cell voltage incorporating thermal effect and concentration overpotential can be expressed as,

$$V_{cell} = \begin{cases} E^\theta(T) + \frac{2RT}{zF} \ln \left(\frac{SOC}{1-SOC} \right) + IR_c + \eta_{con}^+ + \eta_{con}^- & \text{charging} \\ E^\theta(T) + \frac{2RT}{zF} \ln \left(\frac{SOC}{1-SOC} \right) - IR_d - \eta_{con}^+ - \eta_{con}^- & \text{discharging} \end{cases} \quad (20)$$

2.5. State space model

Another definition for SOC in terms of coulomb counting is introduced for the state space model development. SOC is a relative quantity that describes the ratio of the remaining capacity to the nominal capacity of the battery defined as,

$$\text{SOC}(t) = \text{SOC}(0) + \frac{\eta \int I(t)dt}{C_n} \quad (21)$$

where $\text{SOC}(t)$ is the SOC at time instant t , $\text{SOC}(0)$ is the initial value, C_n is the nominal capacity, and $I(t)$ is the current at time t . The current is positive during charge and negative during discharge. In this equation, η is the coulombic efficiency.

By combining the temperature prediction in Eqs. (8)–(12) and with the cell voltage including concentration overpotential in Eqs. (19)–(21), the proposed electrical thermal-dependent model can be expressed in continuous time state space form as below,

$$\dot{x} = Ax + Bu$$

$$y = h(x, u)$$

where the state vector, $x = [\text{SOC} \ \Delta T_s \ \Delta T_p \ \Delta T_t]^T$, the input signal vector, $u = [I(t) \ P_{\text{pump}} \ P_{\text{ch}} \ P_{\text{R}}]^T$,

$$A = \begin{bmatrix} 0 & 0 & 0 & 0 \\ 0 & -\frac{Q_+ + Q_-}{V_s} - \frac{H_s A_s}{C_p \rho V_s} & \frac{Q_+ + Q_-}{V_s} & 0 \\ 0 & \frac{Q_+}{V_p} & -\frac{Q_+ + Q_-}{V_p} - \frac{H_p A_p}{C_p \rho V_p} & \frac{Q_+}{V_p} \\ 0 & 0 & \frac{Q_+}{V_t} & -\frac{Q_+ + Q_-}{V_t} - \frac{H_t A_t}{C_p \rho V_t} \end{bmatrix},$$

$$B = \begin{bmatrix} \frac{\eta}{C_n} & 0 & 0 & 0 \\ 0 & 0 & \frac{1}{C_p \rho V_s} & \frac{1}{C_p \rho V_s} \\ 0 & \frac{1}{C_p \rho V_p} & 0 & 0 \\ 0 & 0 & 0 & 0 \end{bmatrix},$$

$$y = V_{\text{battery}} = \begin{cases} N \cdot \left[E^\theta(T) + \frac{dE}{dT} x(2) + \frac{2RT}{zF} \ln \left(\frac{x(1)}{1-x(1)} \right) + IR_c + \eta_{\text{con}}^+ + \eta_{\text{con}}^- \right] & \text{charging} \\ N \cdot \left[E^\theta(T) + \frac{dE}{dT} x(2) + \frac{2RT}{zF} \ln \left(\frac{x(1)}{1-x(1)} \right) - IR_d - \eta_{\text{con}}^+ - \eta_{\text{con}}^- \right] & \text{discharging} \end{cases} \quad (22)$$

3. Extended Kalman filter method

As stated in the introduction, SOC is usually detected by the OCV using an open circuit flow cell installed in the stack. As for the proposed EKF method, SOC can be estimated by acquired measurable parameters even without the open flow cell. EKF is a quadratic state estimator for a nonlinear system shown in Fig. 4. EKF uses the entire observed data $u(k)$ and $y(k)$ to find the minimum mean

squared error making the estimated state $\hat{x}(k)$ close to the true state $x(k)$. The estimator includes two parts, the battery process part which is a perfect model of the VRB, and the state observer part which is the thermal-dependent electrical model in Section 2.5. By measuring the terminal voltage, $y(k)$ and the input current $I(k)$, the estimated SOC could be obtained. The Kalman gain is utilized to rectify the predicted state. Assuming the discrete nonlinear system is expressed as follows,

$$x(k+1) = A_d x(k) + B_d u(k) + \omega(k)$$

$$y(k) = h(x(k), u(k)) + v(k)$$

where $\omega(k)$ and $v(k)$ are the process noise and measurement noise respectively, obeying zero-mean white Gaussian stochastic process with covariance matrices of Q_k and R_k ,

$$\omega(k) \sim N(0, Q_k), \quad v(k) \sim N(0, R_k)$$

$h(x, u)$ is a nonlinear measurement function.

To facilitate the EKF estimation, the continuous time state space model must be converted to the discrete time one first the following equations,

$$A_d = e^{A \cdot \Delta t}$$

$$B_d = \left(\int_0^{\Delta t} e^{A \cdot \tau} d\tau \right) \cdot B$$

where Δt is the sampling time.

The Extended Kalman filter consists of a set of recursive equations that are repeatedly evaluated as the system operates. The filter steps are summarized as follows [39],

Step I, Initialization: The initial estimation value of \hat{x}_0^- is set according to the best available information based on the state mean and error covariance.

$$\hat{x}_0^- = E(x_0)$$

$$P_0^- = E[(x_0 - E(x_0))(x_0 - E(x_0))^T]$$

Step II, Time update: The expected state value and the state uncertainty at next step are computed.

$$\text{Project the state ahead, } \hat{x}_k^- = A_d \hat{x}_{k-1} + B_d u_{k-1} \quad (23)$$

$$\begin{aligned} \text{Project the error covariance ahead, } P_k^- \\ = A_k P_{k-1} A_k^T + \omega_k Q_{k-1} \omega_k^T \end{aligned} \quad (24)$$

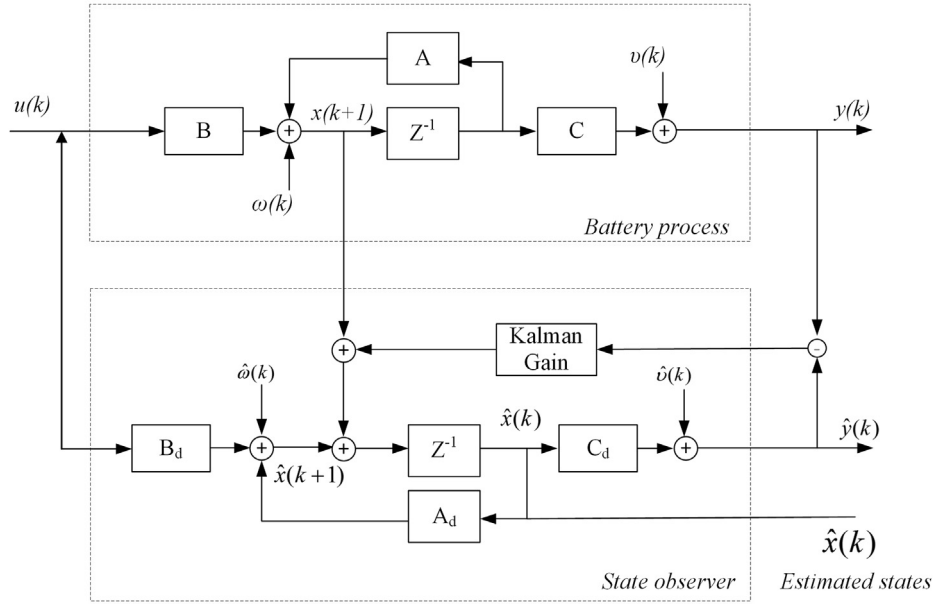


Fig. 4. State estimator with extended Kalman filter.

Step III, Measurement update: The expected state is corrected by Kalman gain to reach a more accurate state. The observed measurement is compared with the expected value and corrected the state and covariance estimation.

At each step, observation matrix is linearized as its Jacobian matrix for nonlinear system,

$$H = \left. \frac{dh(x, u)}{dx} \right|_{x_k = \hat{x}_k} \quad (25)$$

Compute Kalmangain, $K_k = P_k^- H_k^T (H_k P_k^- H_k^T + v_k R_k^- v_k^T)^{-1}$ (26)

Update estimation with measurements, \hat{x}_k (27)

$$= \hat{x}_k^- + K_k (y_k - h(\hat{x}_k^-, 0))$$

Update error covariance, $P_k = (I - K_k H_k) P_k^-$ (28)

The process of the EKF algorithm is summarized in Fig. 5. The iterative process between time update and measurement update starts after the initialization. In this way, SOC can be obtained based on the information of battery terminal voltage, $y(k)$, and input vectors, $u(k)$.

4. Model validation and simulation results

In this section, the proposed thermal-dependent model is validated in three aspects. The simulation results including electrolyte temperatures and stack voltages under various flow rates and applied currents are benchmarked with the experimental data of a kilo-watt class VRB system based on H. Zhang team's published work [40]. Then, the model is adopted in the EKF estimation method to testify the feasibility and accuracy of SOC prediction.

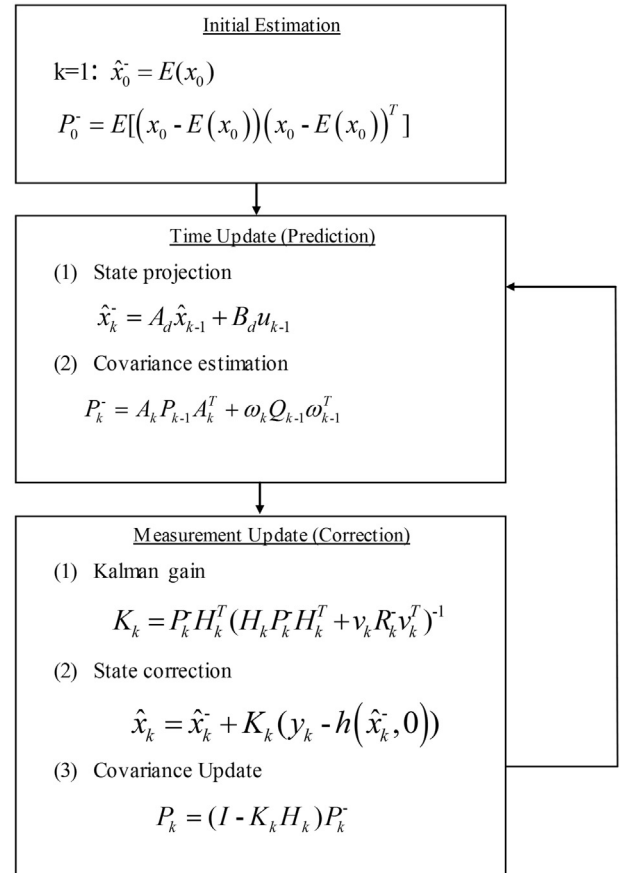


Fig. 5. Flow chart of extended Kalman filter algorithm.

4.1. Temperature effect validation

The ambient condition and the inherent heat generation and convection during operation may vary the electrolyte temperature. Experiments [40–42] were carried out under different ambient temperatures of -5°C , 5°C , 15°C and 25°C with constant charging current density of 40 mA cm^{-2} and discharging current density ranging from 30 to 100 mA cm^{-2} . The electrolyte temperature variation is investigated. The change of electrolyte temperature in the stack under different ambient temperatures is illustrated in Fig. 6(a). The gray area shows the temperature variation region under the described experimental conditions. The specifications of parameters in the model are listed in Table 1. The modeled values in red and blue triangles fit well within the gray area with a mean relative error of 5.85% and root mean square error of 0.86°C , which indicates that the thermal model unit is satisfactory for temperature prediction. From the experimental data, a temperature rise of roughly 10°C is observed in this figure. The voltage variation is simulated in Fig. 6(b) due to the temperature rise according to Eq. (7). The impact of a negative slope of 1.62 mV K^{-1} is found for one single cell owing to the reduction of activation overpotential for a higher temperature. Although the effect is not significant, the error accumulates as the cells are packed in series for large VRB stacks. For a 15 cell stack, the voltage variation reaches to 0.25 V at a temperature rise of 10°C .

4.2. Flow rate effect validation

The flow rate affects the mass transfer rate and thus concentration overpotential, especially when the vanadium species are scarce at the upper or lower limits of SOC. High electrolyte flow rate helps to reduce the concentration overpotential and increases operating capacity. The effect of flow rate was investigated in Ref. [42] and an optimal flow rate strategy was proposed as well. The stack voltage under different flow rates is shown in Fig. 7. With a constant charge/discharge current density of 75 mA cm^{-2} , the experimental data of flow rates under $0.2\text{ m}^3\text{ h}^{-1}$, $0.5\text{ m}^3\text{ h}^{-1}$, and

Table 1

Specifications of parameters in the electrical model.

Symbol	Value
ρ	1400 kg m^{-3}
c	1.5 M
A	875 cm^2
C_p	$3200\text{ J kg}^{-1}\text{ K}^{-1}$
N	$1.78\text{ J K}^{-1}\text{ s}^{-1}$
$H_s A_s$	14
$H_t A_t$	$0.7\text{ J K}^{-1}\text{ s}^{-1}$
$H_p A_p$	$2.07\text{ J K}^{-1}\text{ s}^{-1}$
V_t	7.4 L
V_s	0.6 L
R_c	$0.015\text{ }\Omega$
R_d	$0.024\text{ }\Omega$
Q	$125\text{ cm}^3\text{ s}^{-1}$

$0.7\text{ m}^3\text{ h}^{-1}$ are compared with the simulation results in dotted lines. From this figure, the modeled charging/discharge curves fit well at high flow rate of $0.7\text{ m}^3\text{ h}^{-1}$ with a mean error of 0.06 V , while are less accurate at low flow rate of $0.2\text{ m}^3\text{ h}^{-1}$ with a mean relative error of 0.28 V . It validates the effectiveness of concentration overpotential model in Eq. (19) despite of relative big error at low flow rate. Moreover, the figure suggests that concentration overpotential is sensitive to the flow rate especially when the stack is not well designed due to the large hydraulic resistance.

4.3. Thermal-dependent electrical model validation

After the effect of temperature and flow rate on terminal voltage being analyzed respectively, the overall model performance is verified with the characteristics of a kilowatt VRB at three applied current densities, i.e., 50 mA cm^{-2} , 60 mA cm^{-2} and 70 mA cm^{-2} . The experiment was conducted at a specific ambient temperature and a constant flow rate by Zhao [40]. The results of two models benchmarked with the experimental data in blue circles are shown in Fig. 8 according to Ref. [40]. The model with temperature and concentration effect is plotted in red line while the model without considering temperature and concentration effect is plotted in black curves. The red lines for the proposed model match the experimental data well with the mean error of 0.12 V compared with the black lines with a relatively big error of 0.23 V . Obviously, the two models behave differently at the end of discharge due to the non-negligible concentration overpotential. Thus, the proposed thermal-dependent electrical model is capable of describing the charge/discharge characteristics. The applied current affects the battery behavior as well. The stack terminal voltages vary at different applied currents owing to the voltage loss caused by the internal ohmic resistance. To determine the SOC of VRB, it is not sufficient to be determined with the stack terminal voltage value only. For OCV method, the stack voltage is not used. But for EKF method, the stack voltage is utilized as a key parameter to observe battery state.

4.4. Extended Kalman filter

The performance of EKF estimator is evaluated based on the proposed electrical model in Section 2.5. The experimental data is extracted from Ref. [40] at a constant charging/discharge current density and an initial ambient temperature of 25°C . The continuous state space model is discretized with the sampling time of 0.1 s . Since the EKF method lacks of gain tuning procedures, a large amount of testing is required for the implementation of EKF. The filter covariance matrices are tuned based on trial and error

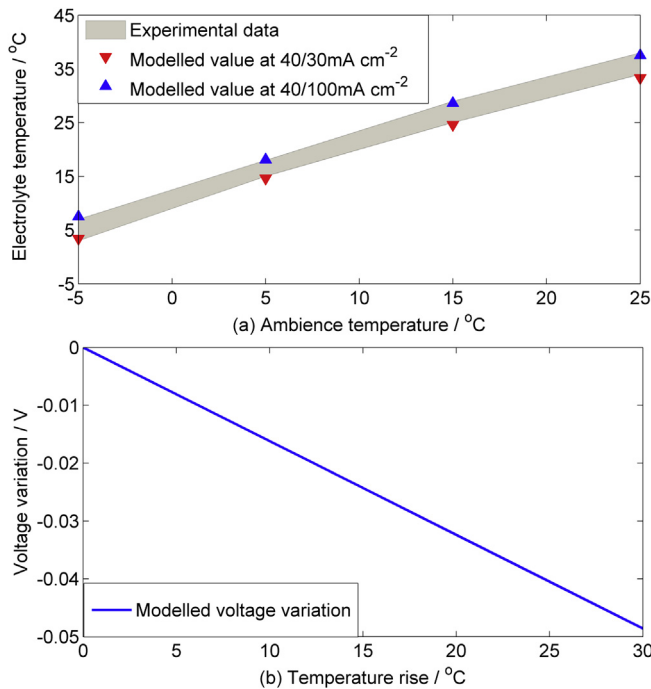


Fig. 6. Electrolyte temperature in stack and voltage variation.

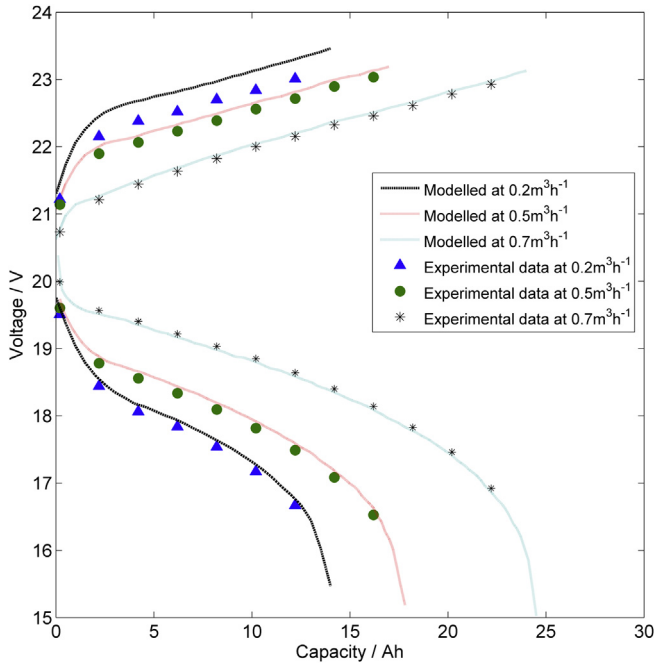


Fig. 7. Stack voltage under various flow rates.

method. To initiate EKF, the following initial values are assigned to the filter,

The covariance of process noise, $R_k = 0.01$,

The covariance of observation noise, $Q_k = \text{diag}(0.02, 0.01, 0.01, 0.01)$,

The predicted covariance, $P_0 = \text{diag}(0.01, 0.01, 0.01, 0.01)$.

By implementing the iteration process according to Fig. 5, the result of SOC estimation is shown in Fig. 9. This figure depicts the estimated SOC and stack voltage and by EKF method. The figure illustrates the relationship between the predicted EKF stack voltage

in the red line, the measured voltage in the black line and the electrical modeled value in the blue line. The battery is operated at a constant current density of 50 mA cm^{-2} for one cycle. The filtered stack voltage tracks the experimental data well despite the modeling error. A root mean square error of 0.034 V with the estimated stack voltage is observed compared with a root mean square error of 0.15 V with the modeled voltage. Since the measurement and prediction noise are not significant in lab testing, the measured voltage keeps high fidelity and the filtered voltage is closer to the measured voltage. A zoom-in view in the middle figure shows the details of the figure above when the mode of battery switches from charge to discharge. It can be seen that the filter achieves better prediction and fast convergence although the filtered stack voltage deviates for several steps due to the disturbance. Fig. 9 shows the estimated SOC and the modeled SOC. The mean difference is 0.033 V which is introduced by the modeling error. It can be concluded that the filtered stack voltage shows better prediction capability.

In the lab testing scenario, process and measurement noises are limited. However, significant noises from converters and PV can be observed when battery is connected online. This may disturb the battery state estimation. Thus, the scenario involving in large amount of noise during battery operation is simulated to test the robustness of EKF method. Experimental data with the random generated white Gaussian noises are generated. The asymmetrical charging/discharging time are applied for battery cycling. The electrolyte temperature change is also observed. Simulation parameters in EKF method are shown in Table 2. The current profile, electrolyte temperature rise, stack voltage and SOC estimation in the noise scenario are shown in Fig. 10. The battery is charged and discharged at a current density of 50 mA cm^{-2} with 45% of charging time and 55% of discharging time in Fig. 10(a). The electrolyte temperature gradually rises up to 6.5°C after about ten cycles due to large amount of heat release. The noise-polluted stack voltage is simulated by the black line while the modeled voltage and filtered one are shown in the blue and red lines respectively. From Fig. 10(c)

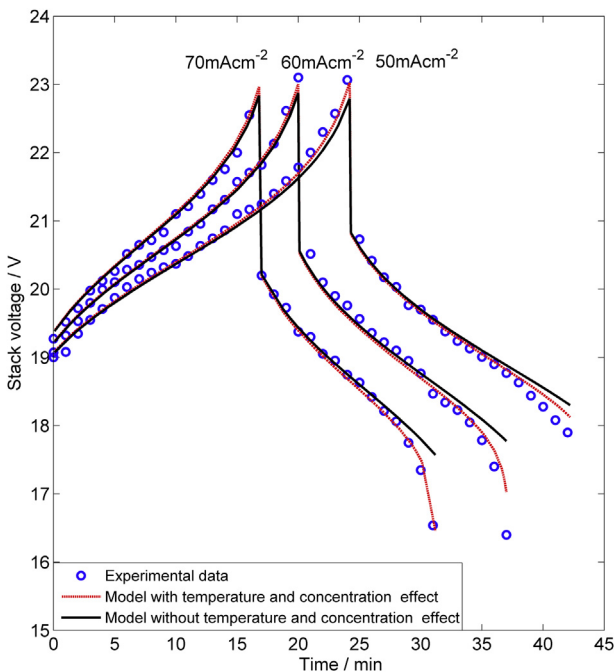


Fig. 8. Thermal-dependent electrical model validation.

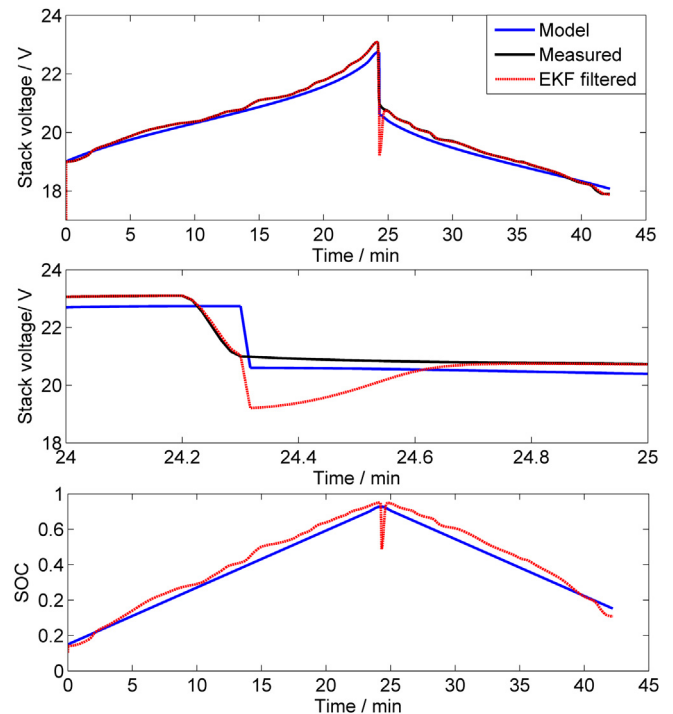


Fig. 9. Stack voltage and SOC estimation by EKF method.

Table 2
Parameters in EKF method.

Parameters	Value
Initial SOC	0.1
Initial process noise covariance	0.01
Initial observation noise covariance	diag(0.01, 0.01, 0.01, 0.01)
Initial predicted covariance	diag(0.01, 0.01, 0.01, 0.01)
Ambient temperature	25 °C
Pump power loss	18 W
Resistive power during discharge	28.7 W
Resistive power during charge	45.9 W
Chemical power release/absorption	16.4 W
Applied flow rate	125 cm ² s ⁻¹
Applied current density	50 mA cm ⁻²
Charging time of one cycle	45%
Discharge time of one cycle	55%

and the zoom-in view of Fig. 10(d), the noise is largely reduced by the filter with the mean error of 0.012 V and the mean squared error of 0.016 V (unit), which shows good noise elimination capability. The variation of SOC estimation by EKF and coulomb counting based model are shown in Fig. 10(e). The SOC gradually decreases due to the relative longer discharge time. The model prediction error increases as the battery operates due to the accumulation of electrical modeling error. A detailed comparison of the SOC error between the model and EKF is given in Fig. 11. The maximum SOC error is within 5.5%.

Another property that EKF possesses is that the accuracy of SOC estimation is independent of the guessed initial SOC. EKF is able to converge SOC to the true value even though the assigned initial value deviates from the real one. In the simulation, the assigned initial SOC is 0.1 while the modeled one is 0.5, which has a large prediction error of 0.4. From Fig. 12, EKF estimated SOC finally reaches to about 0.45 after 8 steps of iteration. The arbitrary initial value assign and fast convergence properties make EKF method

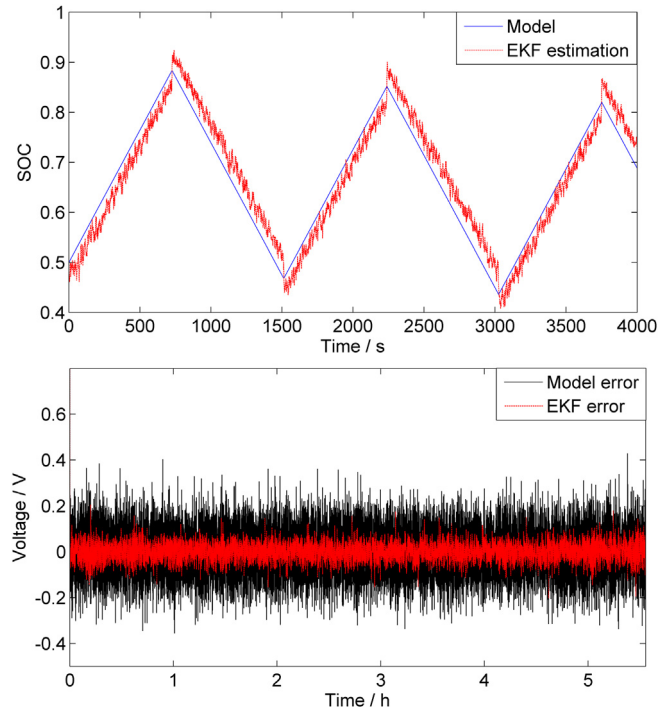


Fig. 11. The error of SOC and voltage between model and EKF.

robust and feasible for SOC estimation in the industrial applications.

5. Discussion

5.1. SOC prediction and stack voltage

In the present electrical model development, the effect of temperature and flow rate have been analyzed and included in the model to make the predicted stack voltage more accurate.

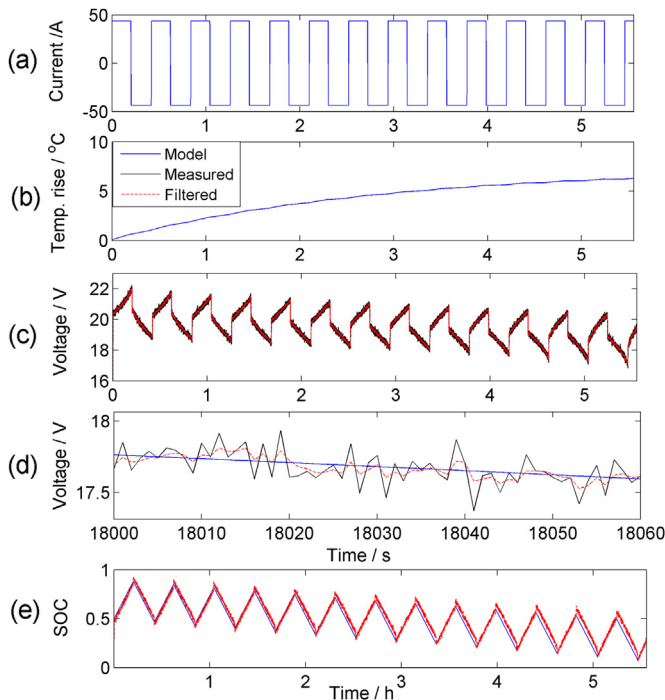


Fig. 10. EKF method estimation: (a) applied current; (b) electrolyte temperature rise; (c) stack voltage; (d) zoom-in stack voltage; (e) SOC estimation.

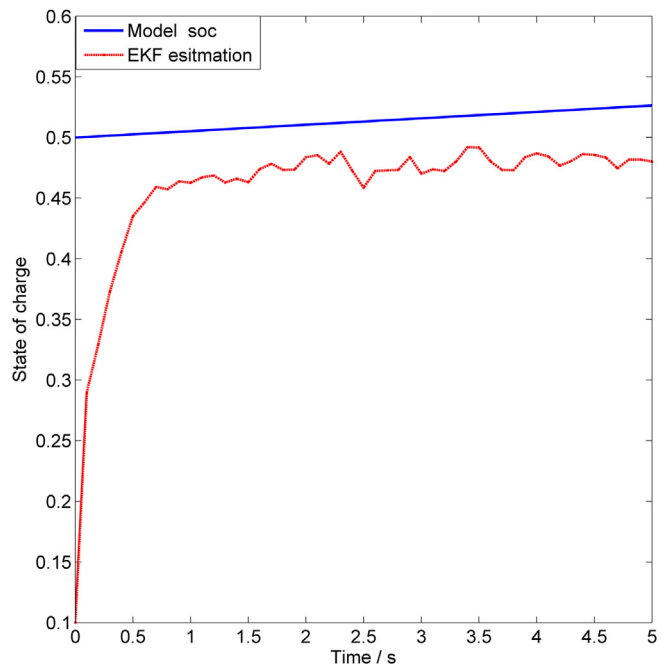


Fig. 12. Initial SOC iteration steps for EKF SOC estimation.

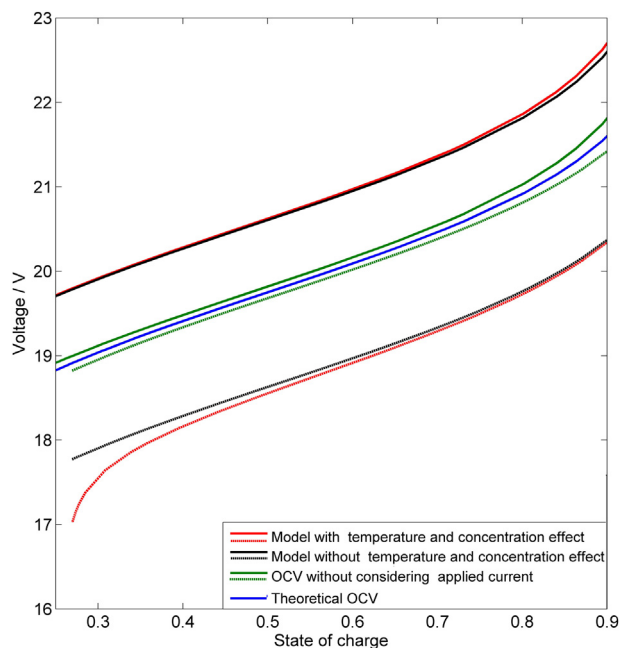


Fig. 13. The relationship between SOC and stack voltage.

Moreover, these effects influence the prediction of SOC as well. In this section, the relationship between predicted SOC and stack voltage under four groups of charging/discharging curves at the current density of 60 mA cm^{-2} is shown in Fig. 13. The stack terminal voltages considering temperature and flow rate effects are shown in red lines. The modeled voltages are close to the experimental data most based on the measured terminal of battery. The modeled stack voltages without these effects in black lines are less accurate than the red line ones, especially at lower or upper limit of SOC due to the flow rate effect. A large SOC prediction error may exhibit when the same level of stack voltage is measured at the end of charging/dischARGE. The green lines without considering the applied currents are utilized in the OCV estimation method. These stack open circuit voltages are not accessible when the batteries are online and are only applicable for the battery testing and modeling. To make OCV estimation method feasible, one single cell needs to be spared in each stack. The slight difference between the green charge/discharge OCV lines is mainly due to the different activation overpotential and the capacity effect during the two processes. The theoretical OCV in the blue line, described in Nernst Equation, is the most accurate one for estimation but the value is not accessible. The SOC estimation methods by applying various voltages are summarized in Table 3.

5.2. Methods comparison

Two methods for SOC estimation, the OCV method and EKF method, are discussed in the introduction part. These two methods

Table 3
Summary of SOC estimation method applying different voltages.

Type	Color	Measurability	Online	Accuracy	Open flow cell
Terminal voltage with effects	Red	Yes	Yes	High	No
Terminal voltage without effects	Black	Yes	Yes	Low	No
Charge/discharge OCV	Green	Yes	No	High	Yes
Theoretical OCV	Blue	No	No	High	Yes

are inherently different. OCV method builds up the predetermined relationship between SOC and the cell open circuit voltage. EKF method utilizes coulomb counting methods on the basis of the electrical model. OCV method needs at least one flow open cell while no such requirement is needed in EKF method. The merits of EKF can be concluded as its initial value independence, fast convergence, noise resistance, and feasible stack terminal voltage access. Meanwhile, EKF stores just one previous step state for the prediction, which saves the computational resources. The disadvantages for EKF method lie in the complexity of the algorithm, and the dependence of electrical model, whereas these are not needed for OCV method.

6. Conclusion

SOC estimation is a critical issue for battery management. Poor SOC estimation may result in over-charging/discharging of the battery. To achieve accurate prediction, an improved electrical thermal-dependent model for VRB is proposed first in this paper. By incorporating the temperature and flow rate effects, the battery model is accurate especially at the end of charging/discharging process. The temperature prediction unit is developed and temperature rise is analyzed based on the energy conversion law in Section 2.2. About 10°C temperature rise is observed. The concentration overpotential unit in terms of flow rate is described in Section 2.3. Later, the overall model is validated with the experimental data at three different current densities with a total mean error of 0.12 V . It indicates that the proposed model shows high accuracy in modeling the battery characteristics over wide range of current densities and SOC. The nonlinear thermal-dependent electrical model is employed for the implementation of EKF algorithm. Two scenarios are tested for the robustness of the method. For the lab testing scenario with limited noise, the stack voltage filtered by EKF tracks well with the experimental data with the root mean square error of 0.034 V . For the online operation scenario in existence of significant noise, the results show that the EKF method reduces the process noise of the model and converge to the real value of SOC within the maximum error of 5.5% . Additionally, the estimator in EKF method allows the estimation of other parameters such as electrolyte temperature if included in the state space.

References

- [1] M. Skyllas-Kazacos, M. Kazacos, J. Power Sources 196 (2011) 8822–8827.
- [2] K.W. Knehr, E.C. Kumbur, Electrochem. Commun. 13 (2011) 342–345.
- [3] M. Skyllas-Kazacos, M. Rychcik, R.G. Robins, A.G. Fane, J. Electrochem. Soc. 133 (1986) 1057–1058.
- [4] M. Rychcik, M. Skyllas-Kazacos, J. Power Sources 22 (1988) 59–67.
- [5] C.P. de Leon, A. Frias-Ferrer, J. Gonzalez-Garcia, D.A. Szanto, F.C. Walsh, J. Power Sources 160 (2006) 716–732.
- [6] M. Skyllas-Kazacos, M.H. Chakrabarti, S.A. Hajimolana, F.S. Mjalli, M. Saleem, J. Electrochem. Soc. 158 (2011) R55–R79.
- [7] M. Skyllas-Kazacos, G. Kazacos, G. Poon, H. Verseema, Int. J. Energy Res. 34 (2010) 182–189.
- [8] A.A. Shah, M.J. Watt-Smith, F.C. Walsh, Electrochim. Acta 53 (2008) 8087–8100.
- [9] H. Al-Fetlawi, A.A. Shah, F.C. Walsh, Electrochim. Acta 55 (2009) 78–89.
- [10] A. Shah, R. Tangirala, R. Singh, R.G.A. Wills, F.C. Walsh, J. Electrochem. Soc. 158 (2011) A671–A677.
- [11] K.W. Knehr, E. Agar, C.R. Dennison, A.R. Kalidindi, E.C. Kumbur, J. Electrochem. Soc. 159 (2012) A1446–A1459.
- [12] M. Vynnycky, Energy 36 (2011) 2242–2256.
- [13] M.R. Mohamed, H. Ahmad, M.N.A. Seman, S. Razali, M.S. Najib, J. Power Sources 239 (2013) 284–293.
- [14] V. Yu, D. Chen, J. Sol. Energy Eng. 136 (2013) 021005–021012.
- [15] A. Tang, S. Ting, J. Bao, M. Skyllas-Kazacos, J. Power Sources 203 (2012) 165–176.
- [16] A. Tang, J. Bao, M. Skyllas-Kazacos, J. Power Sources 216 (2012) 489–501.
- [17] A. Tang, J. McCann, J. Bao, M. Skyllas-Kazacos, J. Power Sources 242 (2013) 349–356.
- [18] S. Corcuera, M. Skyllas-Kazacos, Eur. Chem. Bull. 1 (2012) 511–519.

- [19] L. Liu, J. Xi, Z. Wu, W. Zhang, H. Zhou, W. Li, X. Qiu, J. Appl. Electrochem. 42 (2012) 1025–1031.
- [20] S. Rudolph, U. Schröder, I.M. Bayanov, K. Blenke, D. Hage, J. Electroanal. Chem. 694 (2013) 17–22.
- [21] Z. Tang, D.S. Aaron, A.B. Papandrew, T.A. Zawodzinski, ECS Trans. 41 (2012) 1–9.
- [22] G.L. Plett, J. Power Sources 134 (2004) 252–261.
- [23] G.L. Plett, J. Power Sources 134 (2004) 262–276.
- [24] G.L. Plett, J. Power Sources 134 (2004) 277–292.
- [25] M. Mastali, J. Vazquez-Arenas, R. Fraser, M. Fowler, S. Afshar, M. Stevens, J. Power Sources 239 (2013) 294–307.
- [26] R. Xiong, H. He, F. Sun, X. Liu, Z. Liu, J. Power Sources 229 (2013) 159–169.
- [27] Z. Wei, J. Zhao, M. Skyllas-Kazacos, B. Xiong, J. Power Sources (2014) 89–99.
- [28] C. Chiang, J. Yang, W. Cheng, J. Power Sources 234 (2013) 234–243.
- [29] C. Blanc, Modeling of a Vanadium Redox Flow Battery Electricity Storage System (Phd thesis), EPFL, 2009.
- [30] G. Hwang, H. Ohya, J. Membr. Sci. 132 (1997) 55–61.
- [31] B. Xiong, J. Zhao, K.J. Tseng, M. Skyllas-Kazacos, T.M. Lim, Y. Zhang, J. Power Sources 242 (2013) 314–324.
- [32] A. Heintz, C. Illenberger, Ber. Bunsen. Phys. Chem. 102 (1998) 1401–1409.
- [33] D. Bernardi, E. Pawlikowski, J. Newman, J. Electrochem. Soc. 132 (1985) 5–12.
- [34] A. Tang, J. Bao, M. Skyllas-Kazacos, J. Power Sources 248 (2014) 154–162.
- [35] X. Ma, H. Zhang, F. Xing, Electrochim. Acta 58 (2011) 238–246.
- [36] M. Skyllas-Kazacos, C. Menictas, 19th International Telecommunications Energy Conference, 1997, pp. 463–471.
- [37] A. Parasuraman, T.M. Lim, C. Menictas, M. Skyllas-Kazacos, Electrochim. Acta 101 (2013) 27–40.
- [38] T. Chang, J. Zhang, Y. Fuh, J. Power Sources 245 (2014) 66–75.
- [39] S.X. Chen, H.B. Gooi, N. Xia, M.Q. Wang, Electr. Syst. Transp. IET 2 (2012) 202–210.
- [40] P. Zhao, H. Zhang, H. Zhou, J. Chen, S. Gao, B. Yi, J. Power Sources 162 (2006) 1416–1420.
- [41] C. Sun, J. Chen, H. Zhang, Z. Yang, Battery Bimon. 39 (2009) 297–300.
- [42] X. Ma, H. Zhang, C. Sun, Y. Zou, T. Zhang, J. Power Sources 203 (2012) 153–158.